Electrodeposited nanostructured flakes of cobalt, manganese and nickel-based sulfide (CoMnNiS) for electrocatalytic alkaline oxygen evolution reaction (OER)

Mahesh Verma[1], Lichchhavi Sinha[1], and Parasharam M. Shirage[1,2,*]

[1] *Discipline of Metallurgy Engineering and Materials Science, Indian Institute of Technology Indore, Khandwa Road, Simrol, Indore 453552, India*

[2] *Discipline of Physics, Indian Institute of Technology Indore, Indore 453552, India*

ABSTRACT

The nanostructured flakes of cobalt, manganese, nickel-based sulfide (CoMnNiS) were synthesized by facile electrodeposition technique on Ni foam, for electrocatalytic water splitting. Growth of interconnected flake-like, surface morphology of CoMnNiS was evaluated from field emission scanning electron microscopy (FE-SEM), and its formation has been corelated to metal ion denudated layer (MIDL) theory. Electrocatalytic activities, oxygen/hydrogen evolution were tested in 1 M KOH electrolyte. Oxygen evolution reaction (OER) results revealed a Tafel slope of 48 mV/dec, and overpotential of 371 mV@10 mA/cm^2 with an exchange current density of 0.33 mA/cm^2 (from geometrical surface area). On the contrary, hydrogen evolution reaction (HER) activity exhibited a Tafel slope of 101 mV/dec, and overpotential of $-$ 226 mV@10 mA/cm^2 with an exchange current density of 0.13 mA/cm^2. Stability of CoMnNiS electrocatalyst was tested for 21 h. duration, which demonstrates an efficiency of 48 and 56% for OER and HER process, respectively. These electrocatalytic results are attributed to the presence of electrochemical species (multiple oxidation states of Co, Mn, *i.e.*, Co^{+3}/Co^{+2}, and Mn^{+2}/Mn^{+3}/Mn^{+4}) on the sample surface, as evidenced from X-ray photoelectron spectroscopy (XPS). Thus, the electrodeposited CoMnNiS nanostructure proves to be an effective electrocatalyst in alkaline reaction for OER due to its ease of synthesis, performance, and stability.

Address correspondence to E-mail: pmshirage@iiti.ac.in; paras.shirage@gmail.com

1 Introduction

Need of cost-effective, and efficient electrocatalysts for oxygen/hydrogen generation is highly desirable to exploit hydrogen (H_2) as a source of pollution-free, and green energy [1, 2] through water splitting. Electrocatalysts have potential to replace adverse effect of fossil fuels, like environment pollution by zero carbon emission, and eco-friendly source of renewable energy through hydrogen production by water splitting [3–5]. Many techniques like, photo-chemical, photoelectrochemical, and electrochemical exploits water splitting process. Electrocatalysts depending on their reactivity, reduces the overpotential needed for H_2/O_2 generation, through cathodic hydrogen/anodic oxygen evolution reaction (HER/OER) [2–7], thus facilitating its wide applicability [3, 4]. Mainly, elements like platinum (Pt), and its precious metallic noble group elements like, Ir/Ru serves as an efficient electrocatalyst for HER and OER process, with adversaries like, their cost and availability [3–6]. Therefore, the quest for earth abundant, highly active, and efficient electrocatalysts for HER and OER process is a vital area of research [8, 9]. Transition metal dichalcogenides (TMDs) of the first row and group VI like, Mn, Co, Fe, Ni, V, Mo, etc., and their oxides, nitrides, phosphides, sulfides have been found potentially adequate for HER/OER application in acidic/basic or both medium [10].

Since, HER and OER processes are allied to acidic and alkaline electrolytes by Nernst equation [11], therefore electrocatalysts exhibiting overall water electrolysis in same electrolyte, and cell conditions is highly desirable for sustained H_2/O_2 generation. Moreover, this could ease the environmental factors like, contaminations, cathode–anode material selection, and intricacies in the design of HER/OER catalysts, for simplified cost-effective electrolyzer [11]. In this scenario, bi-functional electrocatalysts possessing copious availability, multi-active sites, and stability features come into play [11–15].

The transition metals elements (TMEs) possess unfilled *d*-orbitals, which make them suitable for electrocatalytic applications [14, 15]. As per Sabatier principle, the binding of an efficient electrocatalyst with reactants/intermediates should neither be too strong nor too feeble, as it leads to inadequate adsorption of species or difficulty in eliminating decisive products [14, 15]. Since OER happens at active sites on the surface of electrocatalyst, therefore

it should have abundance of active sites, further for extraction of electrons at intermediate steps should proceed in fast manner [14, 15]. This property is governed by the conductivity of the sample which TMEs owe naturally [14, 15]. Transition metal nanostructures (TMNs) like, CoMnO@CN (carbon network), NiCoP/CC (carbon cloth), Co_3O_4, CoP, and CoMn [16–18] exhibits HER and OER activity in alkaline electrolyte. TMNs of $NiCoO_4$, NiCoSe and $NiCoMnO_4$ have exhibited superior electrocatalytic activities (alkaline medium), synthesized by various methods like hydrothermal, electrodeposition for electrocatalysis [19–21]. Apart from above, transition metal sulfides (TMS) owning unique physicochemical properties like, low activation energy for electron transfer between cations, high electrical conductivity, presence of multi-valence sites endows electrochemical behavior via donor/acceptor chemisorption sites for adsorption of oxygen [22]. Moreover, doping of multi-metal optimizes the free energy for hydrogen adsorption compared to mono-metal sulfide species for higher HER activity [22]. TMS like, CoNiS [23], NiCoS nanosheets [24], nitrogen-decorated FeNiS, CoMoNiS-NF [25], and others like $MoS_2/Co_9S_8/Ni_3S_2/Ni$ foam synthesized by hydrothermal method depicts the role of multi-metal ion influencing the electrocatalytic properties. Moreover, the DFT studies demonstrate the active site generation in MoS_2 as results of sulfur atoms [22]. High electronegativity of elements offers strong binding of metal atoms and intermediates, an unfavorable condition for efficient electrocatalysts [14, 15]. Electronegativity values of Co (~ 1.88), Mn (~ 1.55), and Ni (~ 1.91) should favor the formation of CoMnNiS structure with tuned electronic structure and optimum bonding, according to Sabatier principle for outstanding catalytic properties. The presence of sulfur could offer amorphous nature with abundant defects generating active catalytic sites for high catalytic performance than their crystalline counterpart [14]. Many works related to Se, S and P induction in the metallic species have been reported, exhibiting high catalytic activity [15]. Many techniques like, electrodeposition, ion exchange, hydrothermal synthesis, etc. have been explored of electrocatalyst synthesis [26–28]. Electrodeposition techniques have an edge over others, being cost-effective, simple, and one step-technique with reproducibility. Morphology and growth of the species are controlled by electrodeposition potential, and bath composition (chemical concentration, pH,

etc.) [29–32]. Electrodeposition allows material formation directly onto the substrate with superior mechanical adhesion [33–35], purity, binder-free and with self-standing approach, thus avoiding demerits of active-site blockage/diffusion during catalytic process [33–37]. Thus, synthesis of multi-metallic (transition metals) species combined with sulfur via electrodeposition could provide insights in material performance and fabrication techniques. Therefore, here we report electrodeposition of combined cobalt, manganese, nickel and sulfur on Ni foam for electrocatalytic application. This nanostructure, CoMnNiS revealed rich redox behavior [38] and is further expected to exhibit increased electrocatalytic activity (HER/OER), for efficient and cost-effective hydrogen/oxygen production.

2 Experimental

2.1 Chemicals

Cobalt nitrate hexahydrate ($Co(NO_3)_2 \cdot 6H_2O$, purity > 97.7% min), manganese nitrate hydrate ($Mn(NO_3)_2 \cdot 6H_2O$, purity > 98%) and nickel nitrate hexahydrate ($Ni(NO_3)_2 \cdot 6H_2O$, purity 98%), were procured from Alfa Aesar. Sodium sulfite (Na_2SO_3, purity 98%) and potassium chloride (KCl, purity 99%) were purchased from Merck. Throughout the experiment double deionized water (DDW) was used, during electrodeposition and electrolyte preparation.

2.2 Material synthesis

Cobalt, manganese and nickel-based nanostructured sulfide (CoMnNiS) was synthesized by electrodeposition technique [38], briefly 0.01 M of $Co(NO_3)_2 \cdot 6H_2O$, 0.01 M of $Mn(NO_3)_2 \cdot 6H_2O$ and 0.01 M of $Ni(NO_3)_2 \cdot 6H_2O$, were dissolved in DDW (30 ml) under constant stirring. Then Na_2SO_3 (0.1 M) and KCl (0.01 M) were added to the above solution under constant stirring. The solution was then transferred, to an electrochemical cell for conducting electrodeposition [38] in three-electrode arrangement. Pre-cleaned Ni foam (1 × 1 cm^2) was used as a working electrode, and Ag/AgCl (saturated, KCl solution) as the reference electrode, and Pt foil as the counter electrode. For electrodeposition − 1.1 V was applied for 3 min duration, with solution temperature

maintained at 85 °C during the process. Electrodeposited Ni foam was then washed with DDW, and later dried overnight at 70 °C for conducting electrochemical studies, electrodeposited mass of the sample was found to be 1 mg.

2.3 Material characterization

The X-ray diffraction (XRD) patterns of bare nickel foam, and electrodeposited CoMnNiS nanostructure were obtained by Rigaku X-ray diffractometer (10° to 80°, step size of 0.02^o and scan rate of 1.8 degree/min) with CuK$_\alpha$ radiation, λ = 1.5146 Å. FE-SEM (Supra 55 Zeiss), and high-resolution transmission electron microscopy (HRTEM), TECNAI F20 Philips operating at 200 kV, were used for analysis of surface morphology and particle size distribution in the sample. Chemical states of various elements present on the surface of sample was detected by X-ray photoelectron spectroscopy (XPS), VG Multilab 2000-Thermo Scientific, USA, K-Alpha equipped with a multi-channel detector, to endure high photonic energies from 0.1 to 3 keV.

2.4 Electrocatalytic measurement

Electrocatalytic measurements of the as-synthesized CoMnNiS nanostructure was conducted in three-electrode cell configuration at 27 °C, using Autolab PGSTAT 302N workstation. Pt sheet and an Ag/AgCl (saturated, KCl solution) electrode were used as counter electrode and the reference electrode, whereas CoMnNiS electrodeposited Ni-foam as a working electrode. Prior to electrocatalytic measurements N_2 gas was purged in the freshly prepared electrolyte 1 M KOH solution for 30 min to remove the dissolved gases. Cyclic voltammetry (CV) tests of 50 cycles at 80 mV/s was conducted prior to electrocatalysis for stabilizing the current. Steady state polarization was conducted at 1 mv/s for electrocatalysis, all measurements were iR corrected to eliminate the influence of uncompensated resistance. Potentials calculated on Ag/AgCl (saturated, KCl solution) scale, were changed to reversible hydrogen electrode (RHE) using relation: E(RHE) = E(Ag/AgCl) + 0.059 × pH + 0.197 V. Overpotential (η) for OER was calculated using the relation: η = E (vs. RHE) − 1.23 V, whereas for HER it was calculated by η = RHE. Tafel slope was calculated from the initial linear region of the plot of Tafel equation:

$\eta = a + b . \log (j/j_o)$ where η, j, j_o, a, and b represent overpotential, current density, exchange current density (calculated from the extrapolation of Tafel plot), a constant and Tafel slope. Onset potential was measured from the initial rise in the electrocatalytic current part of LSV curve. Electrochemical active surface area (ECSA) of the sample was calculated from the electrochemical double layer capacitance (C_{dl}) of electrode, which was evaluated from the cyclic voltammetry (CV) scan, conducted in a non-Faradaic region at different scan rates. Electrochemical impedance spectroscopy (EIS) measurements were conducted in the range of 100 kHz to 0.01 Hz, with an imposed ac voltage of 10 mV in open circuit model at $\eta = 0.55$ and -1.31 V for OER and HER. Long-term stability for OER and HER process for 21 h. duration was examined by chronoamperometric studies carried at fixed overpotentials ($\eta = 0.55$ V and -1.31 V), to record the variation of current density. The overall water splitting was conducted in two-electrode system with symmetric electrodes (cathode and anode) in 1 M KOH solution.

3 Results and discussion

3.1 Nanostructure growth mechanism

The growth of nanostructures on Ni foam by electrodeposition could be explained from the current transient plot shown in Fig. 1. The plot has been divided into three time intervals: (1) in the first
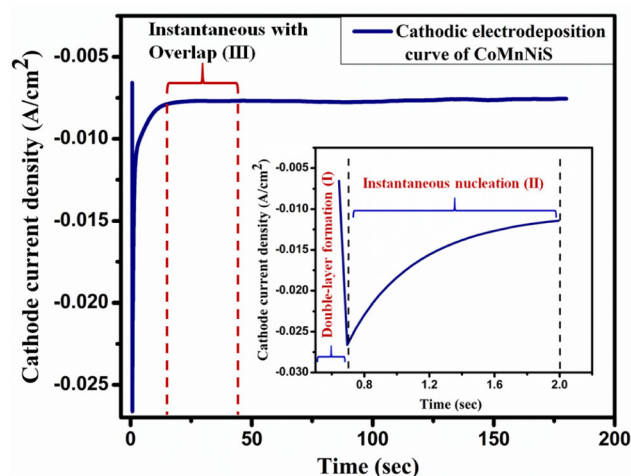
region, current sharply decreases after charging a double layer, representing the formation of first deposition nuclei on the Ni foam surface; (2) in second region the current sharply increases due to an increase in the active surface area of the electrode triggered by the growth of nuclei; (3) slow decrease of the current, representing growth and overlap/formation of an electroactive area, as the diffusion layer at the electrode/electrolyte interface increases [29–32, 37]. This behavior of transient curve is explained by instantaneous and progressive nucleation taking place. The former represents nuclei formation at the commencement of the electric pulse, whereas in the latter simultaneously nuclei are formed along with crystal growth [24, 25, 27, 38, 39]. Peak current corresponds to the overlap of diffusion zones resulting from growing particles, whereas the decreasing current behavior follows the Cottrell equation [38]. Reduction potential applied, and additives [25] used in the process influences the growth of nanostructures, as the concentration of OH^- ions at the electrode is affected by pH of the solution. Therefore, applied field on ions and the reaction kinetics control the deposition of ions on substrate (Ni foam).

3.2 Structural and morphological characterization

The XRD pattern of electrodeposited CoMnNiS nanostructure is shown in Fig. 2a, b. Intensity variation in XRD pattern of the electrodeposited species (on Ni foam), and bare Ni foam could be found from Fig. 2a. Intensity of diffracted peaks of CoMnNiS is less, as compared to the bare Ni foam, suggesting the presence of electrodeposited material. Diffraction peak at 2θ value of 44.70° has been assigned to plane (422) of Co_9S_8, (221) of MnS_2 and (220) of NiS_2; peak at 52.16° to plane (440) of Co_9S_8 and (222) of MnS_2; and similarly, peak at 76.82° to plane (800) of Co_9S_8, (422) of MnS_2, and (421) of NiS_2.

Crystal structure, and the lattice constants of CoMnNiS are matched to Co_9S_8: cubic $a = b = c = 9.928$ Å (JCPDS Card No. 01-073-1442), MnS_2: cubic $a = b = c = 6.091$ Å (JCPDS Card No. 01-076-2049) and NiS_2: cubic $a = b = c = 5.670$ Å (JCPDS Card No. 00-011-0099). Since Co, Mn, and Ni have small difference in their atomic radii [37], therefore their nanostructures with sulfur has less impact on their crystal structure, and overlapping peaks of sulfides of
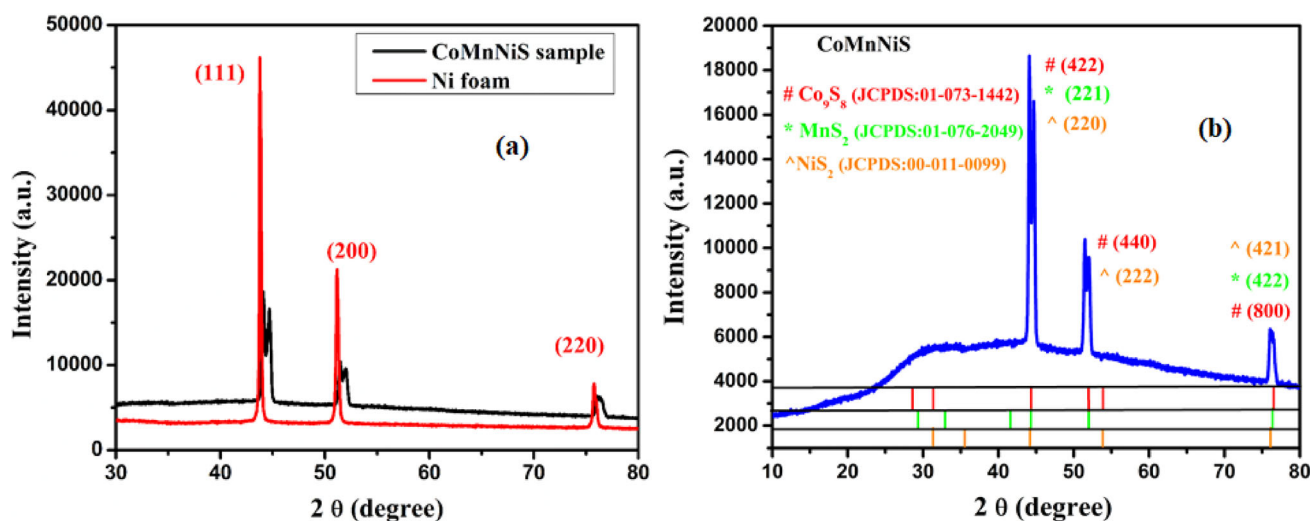

Fig. 1 Transient current vs. time curve for cathodic electrodeposition (chronoamperometry) of CoMnNiS nanostructure on Ni foam at -1.1 V for 3 min duration at 85 °C

Fig. 2 a Comparative XRD pattern of bare Ni foam, and electrodeposited CoMnNiS nanostructure on Ni foam (**b**) diffraction planes of CoMnNiS

Co, Mn and Ni could be seen in the diffraction pattern. CoMnNiS nanostructure is expected to offer multiple oxidation states due to Co, Mn, and Ni favoring electrochemical process [25], thereby leading to enhanced electrocatalytic behavior.

FE-SEM images of CoMnNiS, Fig. 3a–b show interconnected flake-like surface morphology, this nanostructure formation could be referred to the nucleation and growth on 3D Ni foam's irregular surface. The growth of the interconnected vertical nanostructures has been explained by metal-ion denudated layer theory (MIDL) [40]. As the potential is applied to the substrate in electrodeposition, metal ions in close contact to cathode are immediately reduced by electrons present at the cathode. Metal ion discharge process would no longer occur uniformly but takes place preferentially at the pointed (irregular) sites of the substrate. The factors which govern the surface morphology according to MIDL [40] are: (1) applied current density; (2) size of anions in the electrodeposition bath; (3) solution temperature, and (4) agitation of the solution. Low current density favors growth of the rough surface, as compared to high current densities [40]. Small ions like chloride ions, possess low viscosity and promote rough surface, whereas for large ions, its movement towards anode and cathode are interfered, and scatters the discharge phenomenon offering a smooth surface. Anions of small size interfere less, and their discharge is intense on protrusions, thereby creating rough surfaces. In CoMnNiS case, potassium chloride

was used in the electrodeposition bath, which favors the irregular structure formation based on ionic size. High solution temperature produces higher surface irregularities, since the grain size increases with increasing solution temperature, by transfer of metal ions to greater diffusion distance, and by high surface diffusion distance of adatoms [40]. Increased diffusivity permits adatoms to drift a long distance over the surface, thus creating large grains. Solution agitation also affects the surface morphology which makes the surface rough, by influencing the drift of the ions onto the surface of substrate. Such growth of flakes, over and in-plane provides large active surface area with highly porous 3D nanostructure, offering various channels (voids) [25], favoring fast electron transfer from the surface [37] to electrolyte ions leading to efficient electrocatalysis.

HRTEM images, Fig. 3c shows metal sulfide nanoparticles of approximate size 6 nm. Formation of metal sulfide nanostructures are further supported from selected area electron diffraction (SAED) pattern, Fig. 3d showing a polycrystalline nature of CoMnNiS, the two outer most diffraction rings of SAED pattern are indexed to planes (221) and (422) of NiS_2 and MnS_2, whose existence is also supported from XRD.

XPS survey, and high-resolution spectra of electrodeposited CoMnNiS and Co, Mn, Ni, and S are shown in Fig. 4 confirming the existence of Co, Mn, Ni and S in the sample. The 2p peak of Co splits [25] into two i.e., $2p_{3/2}$ (781.2 eV) and $2p_{1/2}$ (797.4 eV)

due to spin–orbit interaction with $\Delta Co = 16.2$ eV. Peak $2p_{3/2}$ is found to be composed of two peaks located at 780.2 and 781.2 eV, which represents the presence of Co^{+3} and Co^{+2} states [27]. The 2p peak of Mn splits into $2p_{3/2}$ (642.3 eV) and $2p_{1/2}$ (653.4), with

Fig. 4 XPS spectra of CoMnNiS nanostructure, showing the ► presence of constituent elements (Co, Mn, Ni, and S) along with their chemical states and functionalities
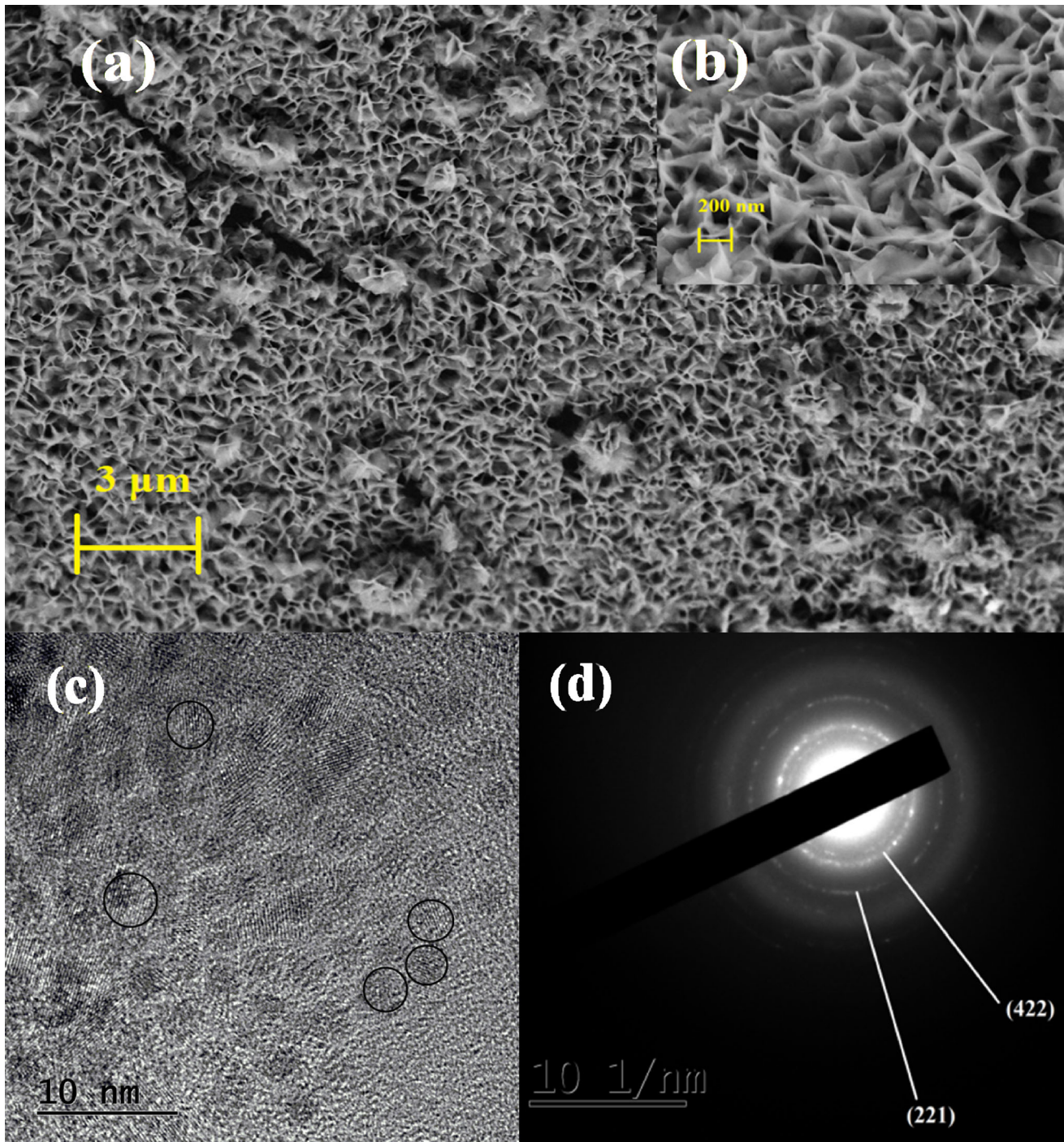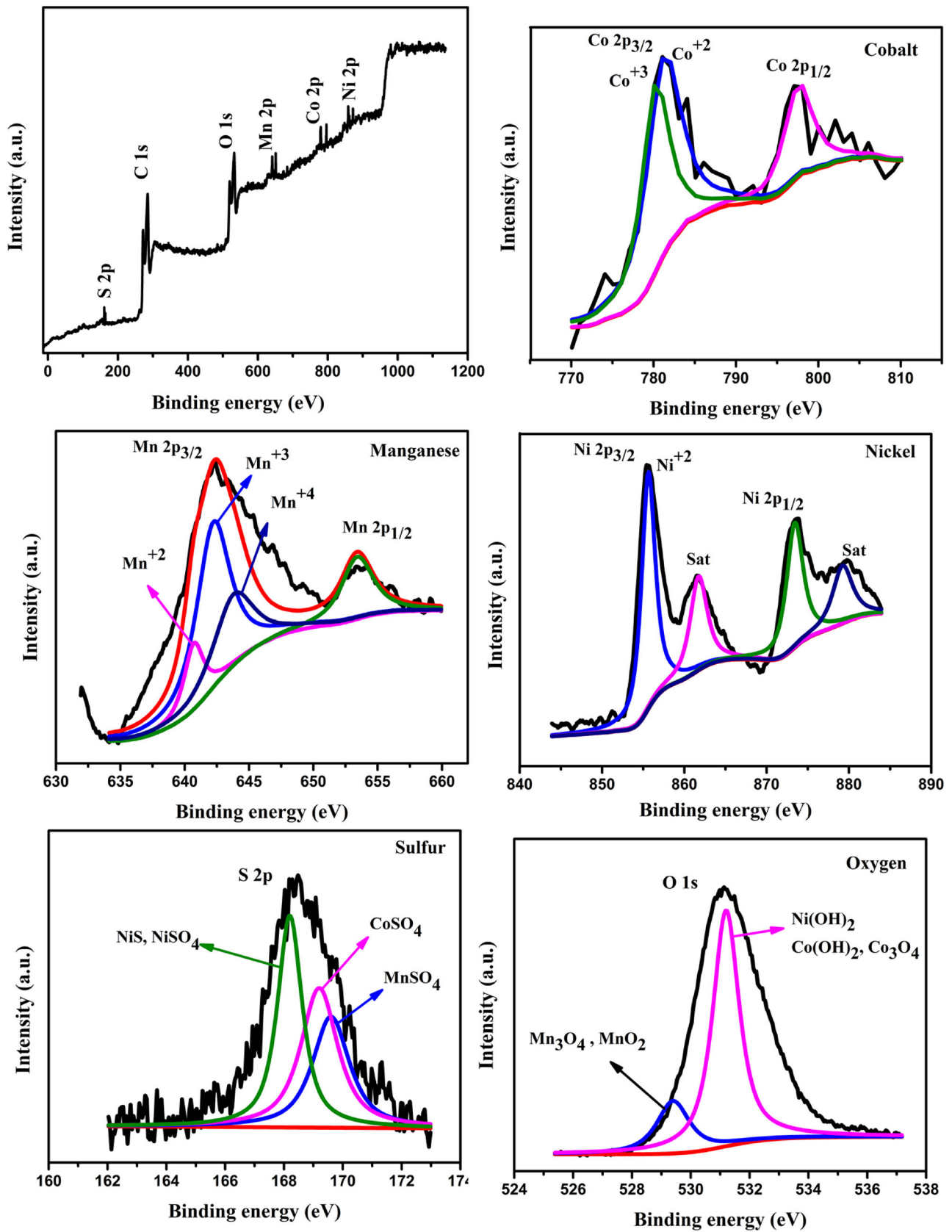

Fig. 3 CoMnNiS nanostructure, **a**–**b** FESEM images showing interconnected nanoflake like morphology at different magnifications (3 μm and 200 nm); HRTEM micrograph, **c** showing metal sulfide nanoparticles in circles, **d** SAED pattern showing diffraction planes, (221) of NiS_2 and (422) of MnS_2
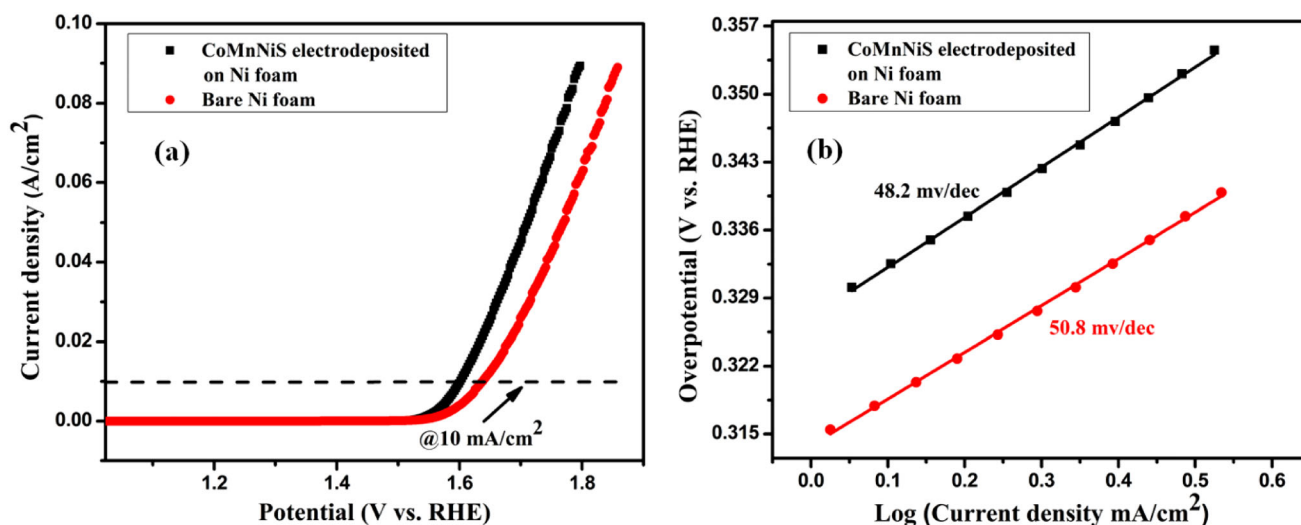
Fig. 5 Steady state polarization curves of CoMnNiS electrocatalyst conducted in 1 M KOH electrolyte **a** OER plot, **b** Tafel plot

Table 1 Representation of values of onset potential, Tafel slope, over potential with exchange current density for OER and HER process for CoMnNiS electrocatalyst, and bare Ni-foam in 1 M KOH electrolyte

Sample	Onset potential, V vs RHE, [mV]		Tafel slope [mV/dec]		η @ at 10 mA/cm^2 V vs RHE, [mV]		Exchange current density [mA/cm^2]	
	HER	OER	HER	OER	HER	OER	HER	OER
CoMnNiS Nanostructure flakes	− 103 @ 5.89 mA/cm^2	283@ 2.01 mA/cm^2	101	48	− 226	371	0.13	0.33
Bare Ni foam	− 198 @ 7.51 mA/cm^2	315@ 5.85 mA/cm^2	112	50	− 320	408	0.22	0.31

$\Delta Mn = 11.1$ eV. Deconvolution of $2p_{3/2}$ peak shows the presence of Mn in Mn^{+2} (640.8 eV), Mn^{+3} (642.3 eV), and Mn^{+4} (644.2 eV) oxidation states, respectively. Multiple oxidation states of Co and Mn specifies oxygen incorporation induced partial electron transfer from Co and Mn to S, which is expected to promote the formation of high-valent Co^{+2}/Co^{+3}, and $Mn^{+2}/Mn^{+3}/Mn^{+4}$ during OER process. This would promote active centers located on the high-valent metal sites [41], thus enhancing the electrocatalytic process [42]. The Ni 2p peak splits into $2p_{3/2}$ (855.7 eV) and $2p_{1/2}$ (873.5 eV), with $\Delta Ni = 17.8$ eV. The $2p_{3/2}$ peak shows a characteristic presence of Ni^{+2}, while satellite peaks of Ni could be located at 861.3 and 879.7 eV, respectively.

The presence of sulfur is confirmed from its 2p peak located at 168.2 eV correspond to residual sulfate groups, or oxidized sulfur species due to surface oxidation [25]. Its deconvolution leads to the confirmation of sulfur with other constituents present in the sample like NiS, $NiSO_4$ at 168.2 eV, $CoSO_4$ at 169.2 and $MnSO_4$ at 169.6 eV, respectively.

Oxygen is confirmed from the O 1 s peak located at 531.2 eV, which shows oxygen attached to Ni and Co in different states like $Ni(OH)_2$, $Co(OH)_2$ and Co_3O_4. The lower part of O 1 s spectrum, 529.4 eV represents oxygen atom bound to Mn, in the form of Mn_3O_4 and MnO_2. Further, the presence of defect oxygen (531.0 eV), hydroxyl group/adsorbed oxygen (531.3 eV), and oxygen adsorbed from H_2O (532.4 eV) is established [42]. The sulfur induced oxygen defects are expected to enhance electrocatalytic activity through modifying the electronic structure around Co^{+2}, and Mn^{+2}/Mn^{+3} during OER. Thereby, enabling high activity for adsorption of H_2O at low-coordinated Co/Mn positions, further the oxygen vacancy induced delocalized electrons are expected to enhance conductivity, by exciting it to conduction band [42].
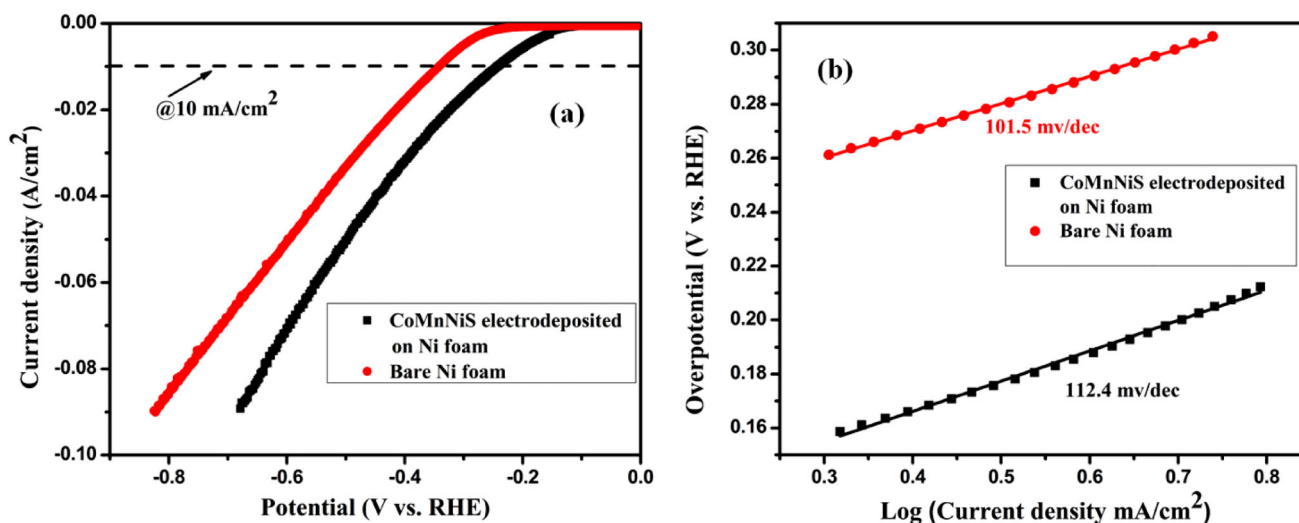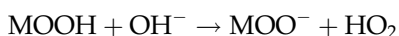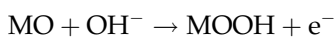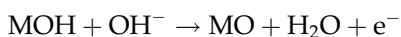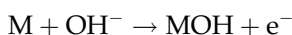
Fig. 6 Steady state polarization curves of CoMnNiS electrocatalyst conducted in 1 M KOH electrolyte **a** HER plot, **b** Tafel plot

3.3 Oxygen and hydrogen evolution activity

Electrocatalytic activities (OER/HER) of CoMnNiS electrode for O_2/H_2 generation, were studied from the steady state polarization curves of electrocatalytic water splitting process. OER polarization curves are shown in Fig. 5a, OER reaction which serves as a half reaction during the water splitting process is a complicated, and slow kinetic process.

OER takes place by four electron transfer process which includes energy loss, breaking of O–H bond, formation of O=O [43], or growth of adsorbed species [43–46]. Many mechanisms have been proposed to explain OER activity, among them Krasil'shchikov's path has a wide acceptance in alkaline medium, and described as under:

$$M + OH^- \rightarrow MOH + e^-$$

$$MOH + OH^- \rightarrow MO + H_2O + e^-$$

$$MO + OH^- \rightarrow MOOH + e^-$$

$$MOOH + OH^- \rightarrow MOO^- + HO_2$$

$$MOO^- \rightarrow M + O_2 + e^-$$

The above complete reaction can be represented by:

$$M + 4OH^- \rightarrow M + O_2 + 2H_2O$$

where M refers to the electrode. CoMnNiS nanostructure demonstrates an onset potential of 283 mV@ 2.01 mA/cm^2 and requires an overpotential of 371 mV@1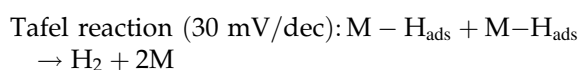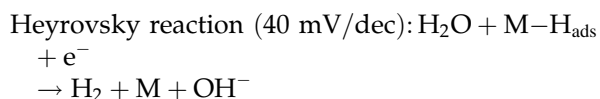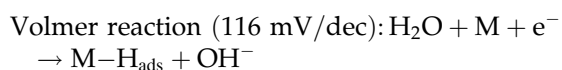0 mA/cm^2, with an exchange current density of 0.33 mA/cm^2. On the contrary, Ni foam shows onset potential of 315 mV@ 5.85 mA/cm^2 and requires an overpotential of 408 mV@10 mA/cm^2 with an exchange current density of 0.33 mA/cm^2, as shown in Table 1. Thus, CoMnNiS nanostructure represents better OER activity than the bare Ni foam. This behavior of nanostructured CoMnNiS is also supported from the FE-SEM, HRTEM, and XPS representing a surface morphology comprised highly interconnected flakes and nanoparticles, with the presence of multi electroactive species. Chemisorption of intermediate species in OER at active sites is greatly influenced by the local electronic structure and electron cloud density, an electrocatalyst must possess low energy electronic fluctuation [15]. Catalytic activity in case of transition metal atoms, is governed by their unfilled d-orbitals, therefore the presence of tri-metal species (Co, Mn, and Ni) is expected to modify the electronic structure, through different d-orbital structure, thereby suppressing the local electronic fluctuations at the active sites [15]. Different metallic species in CoMnNiS offers synergetic effect besides the large electroactive surface sites from ultrathin 3D nanosheets providing large surface area and channels (voids) for fast ion exchange mechanism [25]. Similarly, electrical conductivity [42], and enhanced high valence states of Co and Mn through oxygen incorporation delivers active centers for OER process. Tafel plots generated from Tafel equation (overpotential vs. log (*j*) curve) provides reaction kinetics, mechanism, and rate-determining step of a catalytic process. A Tafel slope of 48 mV/

Table 2 A Comparative data representing electrocatalytic activity of some transition metal/sulfides materials for OER/HER process

Catalyst	OER/ HER	η [mV] @ 10 mAcm^{-2}	Tafel slope [mV dec^{-1}]	Catalyst loading [mg cm^{-2}]	Electrolyte	References
Co$_9$S$_8$/Ni MnS/Ni	HER/ OER	217/298	71.5 100.3	4.1 4.1	1 M KOH	[34]
NiFe@Ndoped carbon	OER	350	56	0.2	0.1 M KOH	[35]
FeNC/NiO	OER	390	76	0.24	1 M KOH	[36]
Ni-MOF@Fe-MOF	OER	265	82	0.2	0.1 M KOH	[49]
Co$_9$S$_8$/NiS@C composites	HER	280	41	5	1 M KOH	[50]
CoSx/Ni$_3$S$_2$@NF	HER	204	133	2.83	1 M KOH	[39]
Ni-Co sulfide	OER	322	52	0.285	1 M KOH	[52]
Co–Fe–S@PB NBs	OER	286	38	20	1 M KOH	[53]
MnO/Co/PGC	OER	307	77	10	1 M KOH	[54]
Co-PBA, Co$_3$[Co(CN)$_6$]$_2$)	HER/ OER	196/298	38/94	–	1 M KOH	[55]
(Co$_3$Mn$_2$)S thin film	OER	243	99	2.36	1 M KOH	[15]
Mn–Co–P yolk-shell	OER	330	59	0.238	1 M KOH	[57]
CoMnNiS	HER/ OER	226/371	101/48	0.2	1 M KOH	Our work

dec was calculated for CoMnNiS electrocatalyst, as compared to 50 mV/dec for Ni foam as shown in Fig. 5b, suggesting its superiority. Tafel slope suggests, that OER in CoMnNiS proceeds with the formation of metal oxide species [46], with fast kinetic process [47–49]. Low values of Tafel slope indicates material's importance as a practical electrocatalyst and favors fast OER process [48–51].

Electrocatalytic HER performance of CoMnNiS electrocatalyst was conducted in steady state polarization, as shown in Fig. 6a. HER process in alkaline medium proceeds via one of the following paths: (1) Volmer reaction; electroreduction of water molecules with hydrogen adsorption (2) Heyrovsky reaction; electroreduction hydrogen desorption (3) Tafel reaction; chemical desorption.

Volmer reaction (116 mV/dec): $H_2O + M + e^- \rightarrow M{-}H_{ads} + OH^-$

Heyrovsky reaction (40 mV/dec): $H_2O + M{-}H_{ads} + e^- \rightarrow H_2 + M + OH^-$

Tafel reaction (30 mV/dec): $M - H_{ads} + M{-}H_{ads} \rightarrow H_2 + 2M$

In the above equations, M and H_{ads} refer to electrode and adsorbed hydrogen at active sites of the catalyst.

CoMnNiS electrocatalyst shows an onset potential of -103 mV@ 5.89 mA/cm^2, and it requires overpotential of -226 mV to achieve a current density of 10 mA/cm^2 with exchange current density of 0.12 mA/cm^2. On the contrary, Ni foam shows an onset potential of -198 mV@7.51 mA/cm^2, and it requires overpotential of -320 mV @10 mA/cm^2 with exchange current density of 0.12 mA/cm^2, as listed in Table 1. A Tafel slope of 101 mV/dec, for CoMnNiS electrocatalyst was obtained, compared to 112 mV/dec for bare Ni foam, thus showing superiority over the later. Tafel results of CoMnNiS electrocatalyst suggests that the completion of reaction follows many paths leading to surface-adsorbed hydrogen [3, 43] species, which is also supported from XPS.

Role of the porosity generated from the 3D arrangement of nanostructured flakes having voids offers plentiful catalytic active sites, enabling fast electron and mass transport for HER, along with the electron-rich S sites [42]. A detailed comparative analysis has been provided in Table 2, between
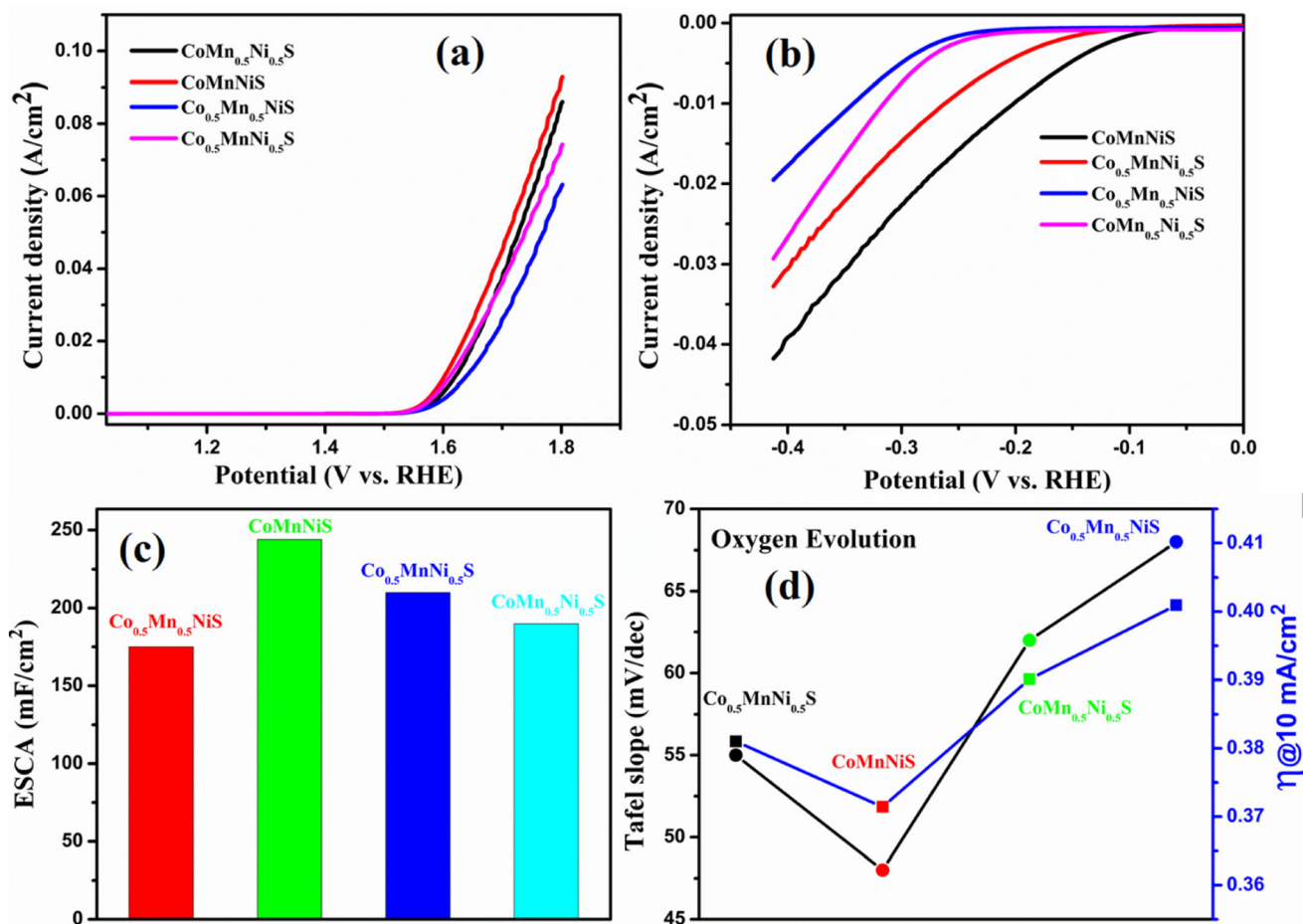
Fig. 7 CoMnNiS, $Co_{0.5}MnNi_{0.5}S$, $CoMn_{0.5}Ni_{0.5}S$, and $Co_{0.5}Mn_{0.5}NiS$ sample. **a–b** Steady state polarization curves of OER and HER. **c** ESCA. **d** Tafel slopes and overpotential values

reported transition metal sulfide, and CoMnNiS electrocatalyst. It could be found that CoMnNiS offers comparable features for electrocatalytic application, along with the ease of fabrication.

The optimization studies of CoMnNiS sample were concluded from the electrocatalytic studies of different samples synthesized by varying the molar concentration of Co, Mn, and Ni, i.e. $Co_{0.5}MnNi_{0.5}S$, $CoMn_{0.5}Ni_{0.5}S$, and $Co_{0.5}Mn_{0.5}NiS$. All these sample were synthesized by the technique reported in the experimental section. These different samples were evaluated on various parameters like, OER/HER characteristics, ESCA (electrochemical surface area), Tafel slope and overpotential values as shown in Fig. 7. Similarly, the values of overpotential and Tafel slope of the CoMnNiS was found to be lower compared to their counterparts as shown in Fig. 7b. Based on these results the superior electrocatalytic behavior of CoMnNiS is established compared to their

counterparts. Combined effect of Co, Mn, and Ni with different electronegativity is expected to influence the polarization of local electron cloud density, leading to optimum electron density for moderate binding strength to intermediates.

The presence of defects, and dangling bonds in TMEs along with sulfur provides atomically disordered amorphous nature to material with abundant active sites. The ESCA results depict the role of surface area exposed to electrolyte for chemisorption of intermediates, further the presence of sulfur offers high active sites, influenced by the chemical environment of material [15]. Thus, a synergetic effect of multi-metals (composition) along with sulfur, and the presence of channels (voids) in the 3D arrangement of nanoflakes lead to enhancement in ESCA and active sites for catalysis.

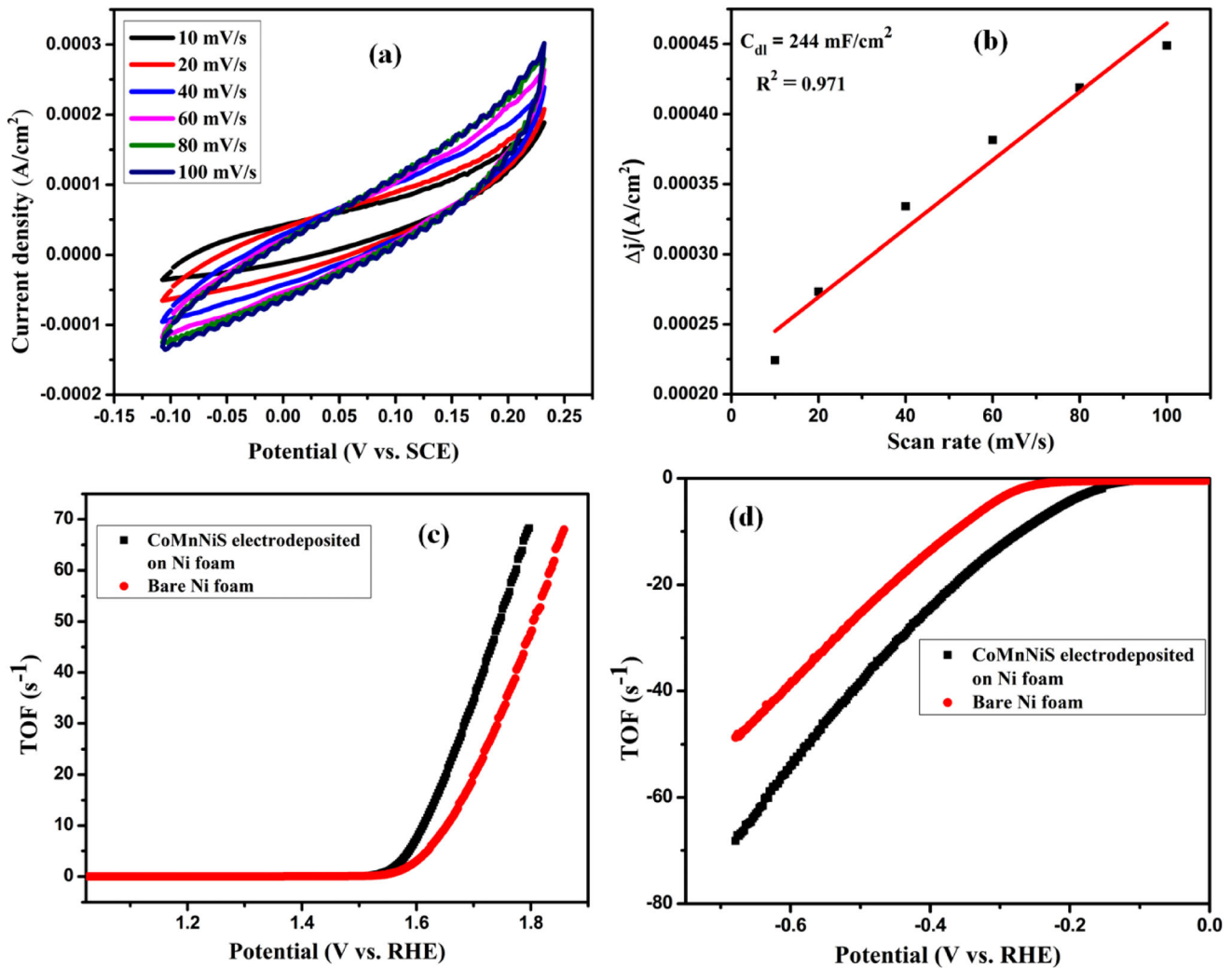Electrochemical active surface area (ECSA) of the sample determines the activity of electrocatalyst,

Fig. 8 a Cyclic voltammetry of CoMnNiS electrocatalyst in non-Faradaic region conducted at different scan rates, **b** determination of double layer capacitance (C_{dl}) from cyclic voltammetry conducted in non-Faradaic region for CoMnNiS electrocatalyst, **c** variation of turn over frequency (TOF) vs. potential (V vs. RHE) of CoMnNiS electrocatalyst and bare Ni foam for OER, **d** Variation of TOF vs. potential (V vs. RHE) of CoMnNiS electrocatalyst and bare Ni foam for HER

which is calculated from the electrochemical double layer capacitance (C_{dl}) of electrode [50]. To get an insight of the active sites [51–57], C_{dl} was evaluated from the cyclic voltammetry (CV) scan conducted in a non-Faradaic region, at different scan rates, and was found to be 244 mF/cm² (Fig. 8a–b).

Further, the turnover frequency (TOF) was evaluated for the ongoing catalytic process using the relation given below [52]:

$$TOF = \frac{J}{2nF}$$

where J (A), F, and n (mol) are current density, Faraday's constant, and no. of active sites of

electrocatalyst which was calculated using following relation:

$$n = \frac{Q}{2F} = \frac{it}{2F} = \frac{iV/v}{2F} = \frac{S}{2Fv}$$

where S is the area of the CV scan shown in Fig. 8a conducted in the non-Faradaic region at scan rate (v) of 40 mV/s, corresponding to it a value of n was calculated: $n = 6.78 \times 10^{-9}$ mol.

The plot of TOF vs. RHE for OER and HER corresponding to CoMnNiS electrocatalyst, and bare Ni foam is shown in Fig. 8c–d. OER mechanism for CoMnNiS electrocatalyst and bare Ni foam shows a TOF of 7.67 and 6.8 s^{-1} @161 mV and 164 mV. On the contrary, TOF values of CoMnNiS electrocatalyst and
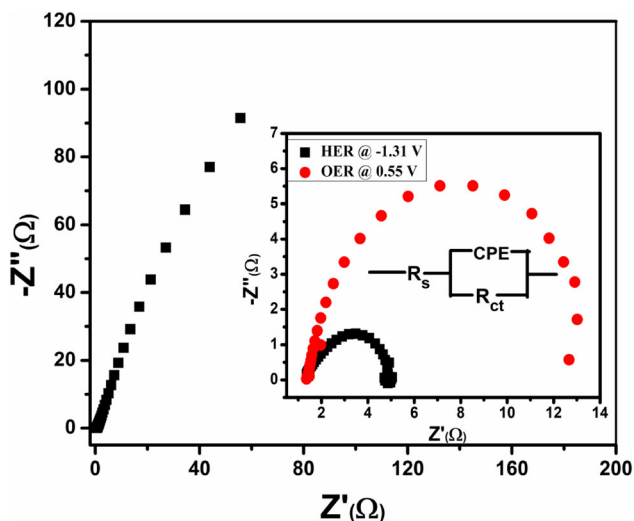
Fig. 9 Nyquist Plot of CoMnNiS electrocatalyst at an open circuit voltage, and at 0.55 V for OER and − 1.31 V for HER process

Ni foam for HER are 7.26, 6.46 s^{-1} and @226 mV and 320 mV. These TOF values demonstrate the superiority of CoMnNiS electrocatalyst to bare Ni foam, for both the OER and HER process which is also supported from previous findings.

Electrochemical impedance spectroscopy (EIS) applies the effect of perturbing ac signal over a constant dc potential to determine the EDL, and rate of OER/HER activity [52]. Based on steady state polarization curve, two dc potentials (0.55 and − 1.31 V) were selected for generating the Nyquist plots, Fig. 9 to determine the charge transfer kinetics. Complete

semi-circular loops were observed at both values of dc potentials for OER and HER, showing an absence of mass transport limitation [53–55].

The diameter of the semi-circular part of Nyquist plot for HER was found to be less than OER, as the later possess increased overpotential and higher ohmic resistance compared to HER. This may be explained based on charge transfer resistance offered for the transfer of hydroxyl group, emerging gas bubbles [53]. Both the Nyquist plots feature a rise at about 45° on higher frequency side, which could be related to the transport resistance of OH^- and suggesting adsorption of OH^- to the nanostructured CoMnNiS as a limiting factor [53]. Randles equivalent circuit was fitted for the above Nyquist plots. The values of series resistance (R_s), constant phase element (CPE) and charge transfer resistance (R_{ct}) were found to be 1.45 Ω, 4.52 mmho and 4.12 Ω for OER process. Similarly, a value of 1.55 Ω, 4.85 mmho and 12.2 Ω was obtained corresponding to R_s, CPE, and R_{ct} for HER process.

A small value of R_{ct} favors electrocatalytic kinetics at the interface of electrolyte, and electrocatalyst for OER for fast electron transfer, as compared to HER, and supported from Tafel slopes corresponding to OER and HER activity.

Stability of electrocatalyst is an important factor governing the evolution of gas from the electrocatalyst surface, under the application of constant overpotential. Stability of CoMnNiS electrocatalyst for OER and HER process was tested in 1 M KOH
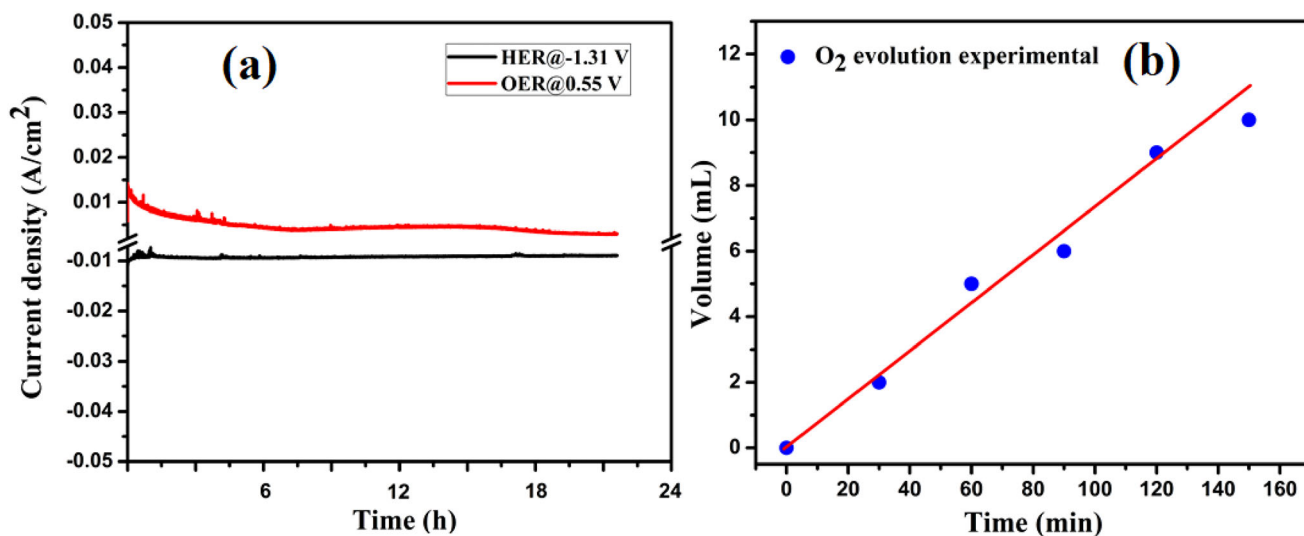

Fig. 10 a Stability plot of CoMnNiS electrocatalyst for OER and HER in 1 M KOH electrolyte for 21 h duration, **b** estimation of oxygen evolution conducted
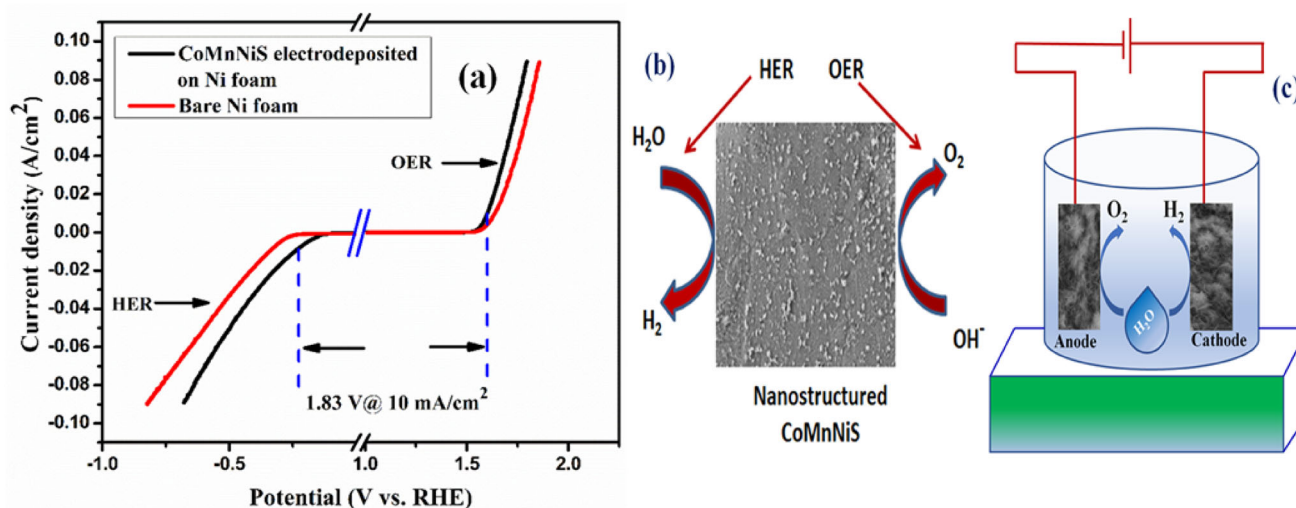
Fig. 11 **a** Overall water splitting process and **b–c** schematic representation for overall water splitting conducted in 1 M KOH electrolyte by CoMnNiS electrocatalyst

electrolyte at a constant overpotential of 0.55 V as shown in Fig. 10a, measured for 21 h. duration. Intake of O^- or accumulation of O_2 onto the electrocatalyst surface i.e., hindering OER [29] could be found in the stability test.

The efficiency of OER process was found to be 48% compared to an initial value of 10 mA/cm^2. Similarly, the stability test conducted for HER process as shown in Fig. 10b, was measured at a constant overpotential of − 1.31 V for 21 h. duration which demonstrates an efficiency of 56%. Small rise in current density could be attributed to the intake of H^- or accumulation of H_2 onto the electrode surface, restricting the gas evolution process [29]. The estimation of the evolved O_2 during OER process was measured by the lateral displacement of the liquid column, results shown in Fig. 10 b, during this period an overpotential of 371 mV (vs. RHE) was applied for 150 min and the corresponding change was evaluated after every 30 min time.

It could be found from the above OER and HER studies that the CoMnNiS electrocatalyst shows best performance as OER catalyst and has comparable features to other HER catalysts [33] as shown in comparative Table 2. Further the evaluation of overall water splitting process conducted in 1 KOH solution as shown in Fig. 11 suggests that CoMnNiS electrocatalyst requires only 1.83 V to achieve a current density of 10 mA/cm^2.

Thus, by utilizing an approach of binder-free electrocatalyst by electrodeposition of Co, Mn, Ni

with S is achieved highlighting the performance of the tri-metallic electrocatalyst. Further the scope exists for reducing the overpotential of CoMnNiS electrocatalyst needed for overall water splitting process.

4 Conclusions

In summary, binder-free nanostructure flakes of Co, Mn, and Ni-based sulfide (CoMnNiS) was grown on Ni foam by electrodeposition technique for electrocatalytic water splitting. XRD and TEM results revealed the presence of cubic phase of Co_9S_8, MnS_2 and NiS_2, i.e. metal (Co, Mn, and Ni) sulfide nanostructure. FE-SEM results revealed interconnected flakes of CoMnNiS which offers large surface area, porosity, and active sites (due to presence of voids, in the interconnected flake region), leading to fast transfer of electrons and ions through metal sulfide nanostructure. Moreover, the presence of multi oxidation states (of Co, Mn, and Ni) as examined from XPS, contribute to electrical conductivity and redox behavior of the sample. These results are also supported from Tafel slopes, and overpotential values for OER/HER activity compared to bare Ni foam. For overall water splitting CoMnNiS electrocatalyst required 1.83 V vs RHE, suggesting its applicability. Most promising attribute of this study is the use of earth abundant material, and facile technique for electrocatalyst fabrication and seeking metal sulfides

as substitutes for noble metal-based electrocatalysts for OER applications.

Acknowledgements

Declarations

Conflict of interest No conflict of interest exists in the submission of this manuscript, and manuscript is approved by all authors for publication.

References

1. J.H. Montoya, L.C. Seitz, P. Chakthranont, A. Vojvodic, T.F. Jaramillo, J.K. Nørskov, Nat. Mater. **16**, 70 (2017)
2. P. Bhojane, L. Sinha, R.S. Devan, P.M. Shirage, Nanoscale **10**, 1779 (2018)
3. Y. Guo, T. Park, J.W. Yi, J. Henzie, J. Kim, Z. Wang, B. Jiang, Y. Bando, Y. Sugahara, J. Tang, Y. Yamauchi, Adv. Mater. **31**, 1807134 (2019)
4. P. Bhojane, A. Sharma, M. Pusty, Y. Kumar, S. Sen, P.M. Shirage, J. Nanosci. Nanotechnol. **17**, 1387 (2017)
5. R.S. Kalubarme, C.J. Park, P.M. Shirage, J. Nanosci. Nanotechnol. **15**, 1253 (2015)
6. X. Zhang, H. Xu, X. Li, Y. Li, T. Yang, Y. Liang, ACS Catal. **6**, 580 (2016)
7. Y. Jiao, Y. Zheng, M. Jaroniec, S.Z. Qiao, Chem. Soc. Rev. **44**, 2060 (2015)
8. J. Wang, W. Cui, Q. Liu, Z. Xing, A.M. Asiri, X. Sun, Adv. Mater. **28**, 215 (2016)
9. P. Xiao, W. Chen, X. Wang, Adv. Energy Mater. **24**, 1500985 (2015)
10. C.C.L. McCrory, S. Jung, I.M. Ferrer, S.M. Chatman, J.C. Peters, T.F. Jaramillo, J. Am. Chem. Soc. **137**, 4347 (2015)
11. B.H.R. Suryanto, Y. Wang, R.K. Hocking, W. Adamson, C. Zhao, Nat. Commun. **10**, 5599 (2019)
12. J. Hou, Y. Wu, B. Zhang, S. Cao, Z. Li, L. Sun, Adv. Funct. Mater. **29**, 1808367 (2019)
13. X. Wang, R. Su, H. Aslan, J. Kibsgaard, S. Wendt, L. Meng, M. Dong, Y. Huang, F. Besenbacher, Nano Energy **12**, 9 (2015)
14. H. Ren, X. Sun, C. Du, J. Zhao, D. Liu, W. Fang, S. Kumar, R. Chua, S. Meng, P. Kidkhunthod, L. Song, S. Li, S. Madhavi, Q. Yan, ACS Nano **13**, 12969 (2019)
15. S.B. Kale, A. Bhardwaj, V.C. Lokhande, D.M. Lee, S.H. Kang, J.H. Kim, C.D. Lokhande, Chem. Eng. J. **405**, (2021)
16. K. Li, J. Zhang, R. Wu, Y. Yu, B. Zhang, Adv. Sci. **3**, 1500426 (2016)
17. J. Li, Y.C. Wang, T. Zhou, H. Zhang, X.H. Sun, J. Tang, L. Zhang, A.M. Al-Enizi, Z. Yang, G. Zheng, J. Am. Chem. Soc. **137**, 14305 (2015)
18. G. Fu, J. Wang, Y. Chen, Y. Liu, Y. Tang, J.B. Goodenough, J.M. Lee, Adv. Energy Mater. **8**, 1802263 (2018)
19. T. Tang, W.J. Jiang, S. Niu, N. Liu, H. Luo, Y.Y. Chen, S.F. Jin, F. Gao, L.J. Wan, J.S. Hu, J. Am. Chem. Soc. **139**, 8320 (2017)
20. X.H. Gao, H. Zhang, Q. Li, X. Yu, Z. Hong, X. Zhang, C. Liang, Z. Lin, Angew. Chem. Int. Ed. **55**, 6290 (2016)
21. Z. Feng, L. Wang, D. Li, S. Gao, Q. Sun, P. Lu, P. Xing, M. An, Nanotechnology **30**, (2019)
22. A. Pendashteh, J. Palma, M. Anderson, R. Marcilla, Appl. Catal. B: Environ. **201**, 241 (2017)
23. G. Fu, J.M. Lee, J. Mater. Chem. A **7**, 9386 (2019)
24. L. Mi, W. Wei, S. Huang, S. Cui, W. Zhang, H. Houb, W. Chen, J. Mater. Chem. A **3**, 20973 (2015)
25. C.V. Manzano, O.C. Calero, S. Hormeno, M. Penedo, M. Luna, M.S. Gonzalez, J. Phys. Chem. C **117**, 1502 (2013)
26. Y. Yang, H. Yao, Z. Yu, S.M. Islam, H. He, M. Yuan, Y. Yue, K. Xu, W. Hao, G. Sun, H. Li, S. Ma, P. Zapol, M.G. Kanatzidis, J. Am. Chem. Soc. **141**, 10417 (2019)
27. H. Wang, A. Hu, M. Li, Cryst. Eng. Commun. **16**, 8015–8019 (2014)
28. Z. Zhang, Y. Liu, L. Ren, H. Zhang, Z. Huang, X. Qi, J. Zhong, Electrochim. Acta **200**, 142 (2016)
29. K. Akbar, J.H. Jeon, M. Kim, J. Jeong, Y. Yi, S.H. Chun, ACS Sustain. Chem. Eng. **6**, 7735 (2018)
30. R.P.M. Shirage, D.D. Shivagan, L.A. Ekal, N.V. Desai, S.B. Mane, S.H. Pawar, Appl. Surf. Sci. **182**, 403 (2001)
31. D.D. Shivagan, P.M. Shirage, S.H. Pawar, Semicond. Sci. Technol. **19**, 323 (2004)
32. P.M. Shirage, D.D. Shivagan, S.H. Pawar, Supercond. Sci. Technol. **17**, 853 (2004)
33. P.M. Shirage, D.D. Shivagan, Y.H. Kim, S.H. Pawar, Appl. Surf. Sci. **253**, 1836 (2006)
34. J. Zhang, T. Wang, D. Pohl, B. Rellinghaus, R. Dong, S. Liu, X. Zhuang, X. Feng, Angew. Chem. Int. Ed. **55**, 6702 (2016)
35. J. Li, W. Xu, J. Luo, D. Zhou, D. Zhang, L. Wei, P. Xu, D. Yuan, Nano Micro Lett. **10**, 6 (2018)
36. Z. Zhang, Y. Qin, M. Dou, J. Ji, F. Wang, Nano Energy **30**, 426 (2016)

37. J. Wang, K. Li, H. Zhong, D. Xu, Z. Wang, Z. Jiang, Z. Wu, X. Zhang, Angew. Chem. Int. Ed. **54**, 10530 (2015)

38. M. Verma, R. Yadav, L. Sinha, S.S. Mali, C.K. Hong, P. Shirage, RSC Adv. **8**, 40198 (2018)

39. S. Dou, L. Tao, J. Huo, S. Wang, L. Daib, Energy Environ. Sci. **9**, 1320 (2016)

40. S. Shit, S. Chhetri, W. Jang, N.C. Murmu, H. Koo, A.C.S. Appl, Mater. Interfaces **10**, 27712 (2018)

41. T. Watanabe, *Nano-Plating Microstructure Control Theory of Plated Film and Data Base of Plated Film Microstructure* (Elsevier, Amsterdam, 2004), p. 14

42. G. Zhang, G. Wang, Y. Liu, H. Liu, J. Qu, J. Li, J. Am. Chem. Soc. **138**, 14686 (2016)

43. G. Anandhababu, Y. Huang, D.D. Babu, M. Wu, Y. Wang, Adv. Funct. Mater. **28**, 1706120 (2018)

44. Q. Sun, Y. Tong, P. Chen, L. Chen, F. Xi, J. Liu, X. Dong, J. Colloid Interface Sci. **589**, 127 (2021)

45. Y. Tong, H. Mao, Y. Xu, J. Liu, Inorg. Chem. Front. **6**, 2055 (2019)

46. C. Hu, L. Zhang, Z.J. Zhao, A. Li, X. Chang, J. Gong, Adv. Mater. **30**, 1 (2018)

47. S. Hyun, S. Shanmugam, ACS Omega **3**, 8621 (2018)

48. S. Hussain, N. Ullah, Y. Zhang, N. Aslam, A. Shaheen, M.S. Javed, M. Wang, G. Liu, G. Qiao, J. Mater. Sci. **30**, 14762 (2019)

49. Z. Ma, Q. Zhao, J. Li, B. Tang, Z. Zhang, X. Wang, Electrochim. Acta **260**, 82 (2018)

50. K. Rui, G. Zhao, Y. Chen, Y. Lin, Q. Zhou, J. Chen, J. Zhu, W. Sun, W. Huan, S.X. Dou, Adv. Funct. Mater. **28**, 1801554 (2018)

51. J. Li, W. Xu, J. Luo, D. Zhou, D. Zhang, L. Wei, P. Xu, D. Yuan, Nano-Micro Lett. **10**, 6 (2018)

52. C. Zequine, S. Bhoyate, K. Siam, P.K. Kahol, N. Kostoglou, C. Mitterer, Surf. Coat. Technol. **354**, 306 (2018)

53. Y.R. Hong, S. Mhin, J. Kwon, W.S. Han, T. Song, H. Han, R. Soc, Open Sci. **5**, (2018)

54. Y. Zhao, C.K. Mavrokefalos, P. Zhang, R. Erni, J. Li, C.A. Triana, G.R. Patzke, Chem. Mater. **32**, 1371 (2020)

55. X.F. Lu, Y. Chen, S. Wang, S. Gao, X.W. Lou, Adv. Mater. **31**, 1902339 (2019)

56. I.K. Ahn, W. Joo, J.H. Lee, H.G. Kim, S.Y. Lee, Y. Jung, J.Y. Kim, G.B. Lee, M. Kim, Y.C. Joo, Sci. Rep. **9**, 19539 (2019)

57. Y.V. Kaneti, Y. Guo, N.L.W. Septiani, M. Iqbal, X. Jiang, T. Takei, B. Yuliarto, Z.A. Alothman, D. Golberg, Y. Yamauchi, Chem. Eng. J. **405**, (2021)